Semiconductor Science and Technology

PAPER

Electrical characteristics and trap signatures for Schottky barrier diodes on 4H-SiC, GaN-on-GaN, AlGaN/GaN epitaxial substrates

To cite this article: Shikha Kumari *et al* 2024 *Semicond. Sci. Technol.* **39** 065016

IOP Publishing

Semiconductor Science and Technology

Semicond. Sci. Technol. **39** (2024) 065016 (12pp)

https://doi.org/10.1088/1361-6641/ad4a65

Electrical characteristics and trap signatures for Schottky barrier diodes on 4H-SiC, GaN-on-GaN, AlGaN/GaN epitaxial substrates

Shikha Kumari[1], Rashmi Singh[1], Shivam Kumar[1], N V L Narasimha Murty[2], Dominique Planson[3], Christophe Raynaud[3], Camille Sonneville[3], Hervé Morel[3], Luong Viet Phung[3], Thi Huong Ngo[4], Philippe De Mierry[4], Eric Frayssinet[4], Yvon Cordier[4], Hassan Maher[5], Raphael Sommet[6], Jean-Christophe Nallatamby[6] and P Vigneshwara Raja[1,*]

[1] Department of EECE, Indian Institute of Technology Dharwad, Dharwad, Karnataka 580007, India
[2] Department of Electrical Engineering, Indian Institute of Technology Tirupati, Tirupati, Andhra Pradesh 517619, India
[3] University Lyon, INSA Lyon, University Claude Bernard Lyon 1, Ecole Centrale Lyon, CNRS, Ampère, Villeurbanne Cedex F-69621, France
[4] Université Côte d'Azur, CNRS, CRHEA, Valbonne 06560, France
[5] Université de Sherbrooke, CNRS-UMI_LN2, Sherbrooke, Quebec J1K 2R1, Canada
[6] XLIM Laboratory, CNRS, UMR 7252, University of Limoges, F-19100 Brive, France

E-mail: vigneshwararaja@iitdh.ac.in

Received 23 February 2024, revised 31 March 2024
Accepted for publication 2 May 2024
Published 21 May 2024

CrossMark

Abstract

The forward and reverse current transport mechanisms, temperature dependence of Schottky barrier height (SBH) and ideality factor, barrier inhomogeneity analysis, and trap parameters for Schottky barrier diodes (SBDs) fabricated on 4H-SiC, GaN-on-GaN and AlGaN/GaN epitaxial substrates are reported. High SBH is identified for Ni/4H-SiC (1.31 eV) and Ti/4H-SiC (1.18 eV) SBDs with a low leakage current density of $<10^{-8}$ A cm^{-2} at -200 V. Thermally stimulated capacitance detects the well-known $Z_{1/2}$ electron trap at E_C—0.65 eV in both 4H-SiC SBDs, while an additional deep-level trap at E_C—1.13 eV is found only in Ni/4H-SiC SBDs. The vertical Ni/GaN SBD exhibits a promising SBH of 0.83 eV, and two electron traps at E_C—0.18 eV and E_C—0.56 eV are identified from deep-level transient Fourier spectroscopy. A peculiar two-diode model behavior is detected at metal/GaN/AlGaN/GaN interface of high-electron mobility transistor (HEMT); the first diode (SBH-1 of 1.15 eV) exists at the standard Metal/GaN Schottky junction, whereas the second diode (SBH-2 of 0.72 eV) forms due to the energy difference between the AlGaN conduction band and the heterojunction Fermi level. The compensational Fe-doping-related buffer traps at E_C—0.5 eV and E_C—0.6 eV are determined in the AlGaN/GaN HEMT, through the drain current transient spectroscopy experiments.

Keywords: Schottky barrier diode, 4H-SiC, GaN, HEMT, current transport, traps

* Author to whom any correspondence should be addressed.

1. Introduction

A good quality Schottky barrier diode (SBD) demands large Schottky barrier height (SBH), high forward current with low voltage drop, low reverse leakage current, high breakdown voltage, and minimal trapping in the epilayer. In practice, the SBH value is determined by the metal work function and the Fermi level pinning effect [1–4]. Low SBH (<0.6 eV) can only be obtained with Si-based SBDs, resulting in high leakage current, low breakdown voltage ($V_R > -100$ V), and off-state power dissipation [5]. For this reason, silicon PiN diodes are preferred for power rectifier applications over SBD structures [5]. On the other hand, high breakdown voltage ($V_{BR} > 1$ kV), large SBH ($\Phi_B > 1.3$ eV), and low leakage current density can be attained using a simple 4H-silicon carbide (4H-SiC) SBD structure, due to the wide bandgap (3.26 eV), high breakdown field, and superior thermal conductivity of 4H-SiC. The 4H-SiC SBD rectifiers have already replaced the silicon PiN diodes up to the voltage range of 5 kV [5]. Ni-based Schottky contacts are widely used on the n-type semiconductors because of its high metal work function (5.15 eV), low price, high thermal stability, good adhesion, and stable nickel silicide formation. Ti-based Schottky contacts on 4H-SiC have also shown promising results ($\Phi_B > 1.1$ eV) for rectifier applications [6]. Commercial semiconductor foundries like ON semiconductor employ Ti-based Schottky contacts in their SiC SBD structure [7]. Since Ni- and Ti-based Schottky contacts are utilized in 4H-SiC devices technologies, the Ni/4H-SiC and Ti/4H-SiC SBDs are used for this study.

Gallium nitride (GaN) is another attractive wide bandgap semiconductor (3.4 eV) suitable for mid-range power applications (currently up to 600 V) [8]. The availability of GaN-on-GaN homoepitaxial substrates has given momentum to the device community for developing vertical GaN power devices. Accordingly, vertical Ni/GaN SBD properties are investigated in this work. The AlGaN/GaN high-electron mobility transistor (HEMT) devices are recommended for the RF and microwave electronic systems [8]. Nevertheless, the gate leakage current induces off-state and standby power dissipation, limited gate voltage swing, and undermines the transistor reliability. The gate leakage current must be minimized to improve the off-state HEMT performance [9]. So, the gate current-voltage (I_G–V_G) characteristics of the AlGaN/GaN HEMT are analyzed at $V_{DS} = 0$ V condition, to understand the gate leakage transport.

Although extensive reports are available on SBD electrical characteristics [9–15], this work systematically investigates the electrical properties of the SBDs fabricated on the different epitaxial substrates (4H-SiC, GaN-on-GaN, and GaN/AlGaN/GaN on SiC) as follows: the current transport processes responsible for the forward and reverse current density are determined by fitting the experimental data. The spatial homogeneity of the barrier is evaluated through temperature-dependent SBH and ideality factor (n). The effective SBH is computed from the conventional and modified Richardson plots. T_0 anomaly ($n = 1 + T_0/T$) is estimated for non-ideal SBDs. Specifically, a peculiar two-diode model characteristic is detected at metal/GaN/AlGaN/GaN interface of the HEMT. So, this study may provide a complete understanding of the SBD electrical properties of the emerging SiC and GaN semiconductors.

The electrically active traps in the SBD induce charge trapping and detrapping effects during the diode operation. Notably, the traps with deeper energy and higher concentration could reduce the diode forward current, and increase the on-state voltage drop, series resistance (decreasing mobility), and leakage current, thereby degrading the SBD properties [5, 6]. Thus, the crystal growth and device scientific communities should know the trap signatures (energy level, trap concentration, and capture cross-section) in device to improve the epilayer crystalline quality. In this work, traps in the Ni/4H-SiC SBD, Ti/4H-SiC SBD, Ni/GaN SBD, and AlGaN/GaN HEMT are identified by various characterizations (TSCAP/DLTFS/DCTS). The reported trap parameters can be used to model the trapping-induced changes in the electrical characteristics of the SBDs in commercial device simulators.

2. Experiment

2.1. SBD and HEMT details

The fabrication steps for 4H-SiC SBDs, and Ni/GaN SBDs are described elsewhere [16, 17]. The schematic cross-sectional diagrams for (a) Ni/4H-SiC SBD, (b) Ti/4H-SiC SBD, (c) vertical Ni/GaN SBD, and (d) GaN/AlGaN/GaN HEMT are depicted in figure 1. The room-temperature epitaxial layer resistivity of 4H-SiC and GaN-on-GaN wafers is estimated 6.25 Ω cm, and 0.45 Ω cm, respectively.

In Ni/4H-SiC SBDs, 200 nm thick Ni metal layer was chosen for top Schottky contact, and Ti/Au (50 nm/150 nm) bilayer was used for bottom Ohmic contact. After Ni deposition, the samples underwent for thermal annealing at 450 °C for 30 min in Ar ambient. In Ti/4H-SiC SBDs, the same Ti/Au (50 nm/150 nm) bilayer was employed for the Schottky contact on the lightly-doped epilayer, as well as the Ohmic contact on the highly-doped back surface. Both the contacts were not annealed in Ti/4H-SiC SBDs. The active area of the Ni/4H-SiC and Ti/4H-SiC SBDs was 3.8×10^{-2} cm^2.

In vertical Ni/GaN SBDs, Ni/Au (40 nm/200 nm) bimetal layer was considered for the top Schottky contact (200 μm diameter) and the Ti/Al/Ni/Au (30 nm/180 nm/40 nm/200 nm) metal stack was employed for the back Ohmic contact. 200 nm thick Au contact pad was placed on top contact. After metal depositions, no annealing was done in the Ni/GaN SBDs. The active area of the Ni/GaN SBD was 3.14×10^{-4} cm^2.

The HEMT device was developed on GaN/AlGaN/GaN heteroepitaxial layer grown on a semi-insulting SiC substrate. The Fe-doping was incorporated into the buffer layer. The Ni/Au bilayer was utilized for the gate Schottky contact, and the regular Ti/Al/Ni/Au-based Ohmic contact was selected for the source and drain electrodes. The silicon nitride (SiN) passivation layer was incorporated in the ungated region of the AlGaN/GaN HEMT structure. The gate length (L_G) and width (W_G) of the HEMT were 0.15 μm and 200 μm, so the active area (A) of the Schottky gate diode is 3×10^{-7} cm^2.

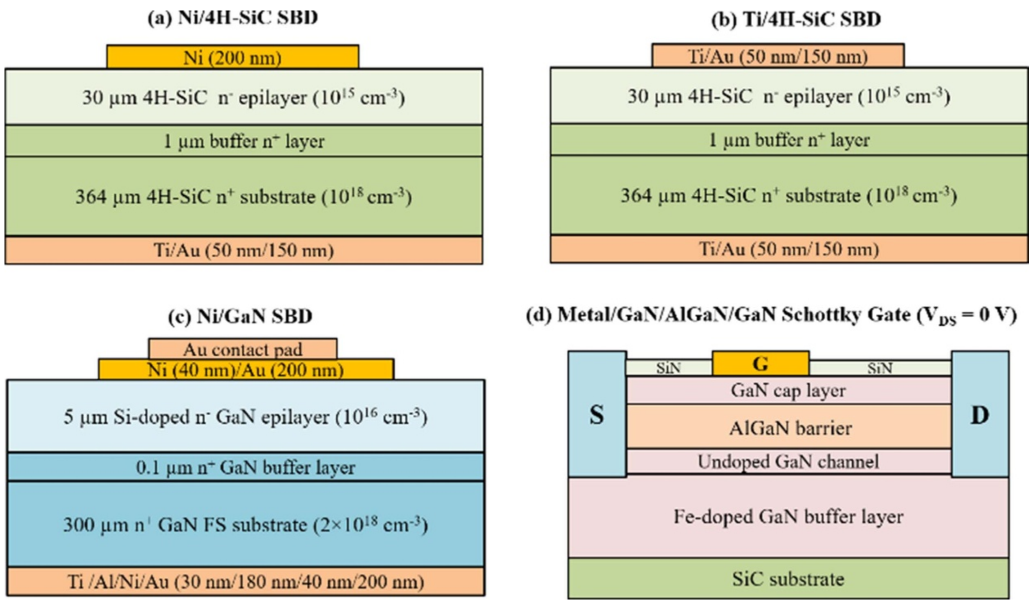

Figure 1. Schematic cross-section for (a) Ni/4H-SiC SBD, (b) Ti/4H-SiC SBD, (c) Ni/GaN SBD, and (d) GaN/AlGaN/GaN HEMT.

2.2. *Electrical characterization*

At first, the forward and reverse I–V characteristics of the SBDs were measured at room temperature. Then, the I–V experiments were conducted at different temperatures (from 300 K to 450 K) by varying the sample chuck temperature of the probe station, i.e. current-voltage-temperature (I–V–T) characterization. The gate current-voltage (I_G–V_G) characteristics of the HEMT were measured at zero drain voltage ($V_{DS} = 0$ V), to investigate the gate diode properties.

2.3. *Trap characterization*

The traps in the Ni/4H-SiC and Ti/4H-SiC SBDs were identified by the thermally stimulated capacitance (TSCAP) spectroscopy. At a low temperature of 120 K (T_f), the majority carrier (electron) traps were filled by forward biasing the SBD. After that, sample temperature was increased, and variation in the diode depletion capacitance was measured at a fixed reverse voltage (-40 V) for temperatures ranging from 120 K to 650 K.

Deep-level transient Fourier spectroscopy (DLTFS) procedure was used to characterize the traps in the vertical Ni/GaN SBDs. During the DLTFS thermal scan (40 K to 460 K), the traps in the diode are periodically populated by reducing the reverse bias from -5 V to -0.1 V with 100 μs pulse width. At the end of the filling pulse, capacitance emission transients were recorded at -5 V in regular temperature intervals. Since DLTFS software computes the discrete Fourier coefficients for each transient, the emission time constant of the trap was directly extracted from a single DLTFS thermal scan.

The traps in the AlGaN/GaN HEMT were detected by the isothermal drain current transient spectroscopy (DCTS) technique. At a fixed temperature, trap filling was achieved by pulsing V_{DS} from 10 V to 20 V for 100 ms duration. Successively upon the filling pulse, drain current emission transients were measured at 10 V over the time interval of 1 μs to 1 s. The isothermal DCTS experiments were performed at five different temperatures (300 K, 325 K, 350 K, 375 K, and 400 K) to calculate the trap signatures using the Arrhenius relation.

3. Results and discussion

3.1. *Ni/4H-SiC SBDs*

The forward current density-voltage (J_F–V_F) characteristics of the Ni/4H-SiC SBD are shown in figure 2(a). At low forward voltages ($V_F < 0.38$ V), a substantial potential barrier existing at the metal/semiconductor junction retards the electron emission over the barrier, so tunneling current transport (J_{TU}) is estimated for J_F up to 0.38 V, based on the following expression [2]

$$J_{TU} = J_{T0}\left(\frac{q\left(V_F - I_F R_s\right)}{\eta E_0}\right) \tag{1}$$

where J_{T0} is the tunneling saturation current density, η is the fitting parameter, and E_0 defines the barrier transparency during the tunneling [1]. Beyond $V_F > 0.38$ V, the electrons may surmount the barrier, so the standard thermionic emission (TE) model (J_{TE}) governs J_F, as predicted by [1, 11, 15]

$$J_{TE} = J_s\left[\exp\left(\frac{q\left(V_F - I_F R_s\right)}{nkT}\right) - 1\right] \tag{2}$$

$$J_s = A^* T^2 \exp\left(-\frac{q\Phi_B}{kT}\right) \tag{3}$$

where V_F is the forward voltage, I_F is the forward current, q is the electronic charge, R_s is the series resistance, J_s is the saturation current density, A^* is the Richardson's constant

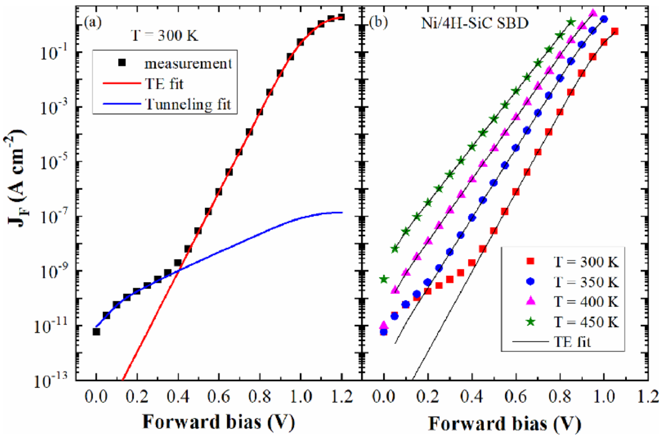

Figure 2. (a) TE and tunneling components in J_F–V_F characteristics of Ni/4H-SiC SBD at 300 K. (b) J_F–V_F at different temperatures (300 K to 450 K) is fitted with the TE model.

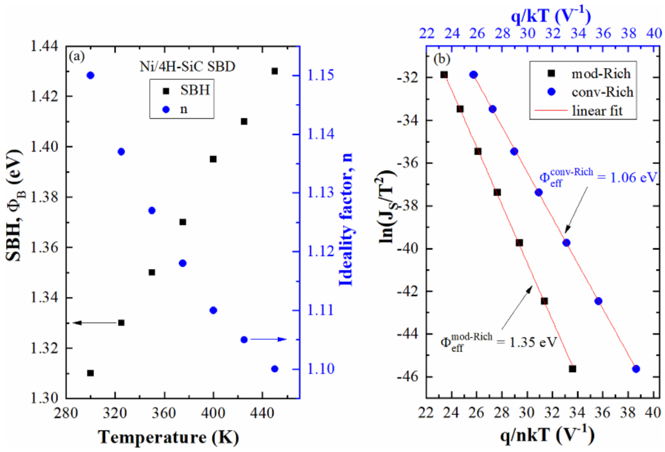

Figure 3. (a) Temperature induced variations in SBH and *n* of the Ni/4H-SiC SBDs. (b) The conventional and modified Richardson plots for computing effective SBH (Φ_{eff}) of Ni/4H-SiC SBDs.

(146 A cm^{-2}K^{-2} for 4H-SiC) [6], k is the Boltzmann constant, and T is the temperature. The SBH (1.31 eV) and n (1.15 at 300 K) values for Ni/4H-SiC SBDs are calculated from linear region of $ln(J_F)$-V_F plot, using the TE equations (2) and (3).

Equations (1)–(3) designate that J_{TE} should augment with the increasing temperature, while the tunneling is a temperature-independent process [1]. Figure 2(b) shows that the TE model essentially controls the J_F characteristics at higher temperatures ($T > 350$ K) in the entire voltage range. The voltage drop across the SBD (V_{ON}) at 10 mA cm^{-2} (0.88 V at 300 K and 0.64 V at 450 K) is found to reduce with the temperature due to the decrease in the built-in barrier potential (V_{bi}). The increased temperature shifts the Fermi level (E_F) toward the mid-gap energy due to the augmented intrinsic carrier concentration (n_i), which increases the semiconductor work function (ϕ_s, energy difference between E_F and vacuum level increases) [1]. Consequently, V_{bi} decreases at higher temperatures, as per the Schottky–Mott theory equation $qV_{bi} = q\ (\phi_m$-$\phi_s)$ [1–3], where ϕ_m is the metal work function.

Figure 3(a) displays the variation in the SBH and n of the Ni/4H-SiC SBDs in the temperature range of 300–450 K. It is noticed that SBH increases with the temperature (1.31 eV at 300 K, 1.37 eV at 375 K, and 1.43 eV at 450 K), as conflicting with the expected SBD properties. In general, the electron affinity (χ) of the semiconductor increases with the temperature due to the bandgap narrowing effect [1]. As a result, the SBH should decrease with the temperature, according to the expression $q\Phi_B = q\ (\phi_m$-$\chi)$. Moreover, the electron kinetic energy upsurges with the temperature, promoting the thermionic field emission (TFE). Hence, the TFE current density (J_{TFE}) may be comparable with the J_{TE} component at higher temperatures [1, 3]; if this is the case, the ideality factor should increase with the temperature. On the contrary, the ideality factor of the Ni/4H-SiC SBD decreases with increasing temperature (1.15 at 300 K, 1.118 at 375 K, and 1.1 at 450 K). Thus, the TE current is predominant (relative to TFE) even at high temperatures in the Ni/4H-SiC SBDs. However, this temperature dependency of the SBD parameters (Φ_B increases and n decreases) is often ascribed to the non-ideal SBD properties [10]. Moreover, spatial variation in the SBH (barrier inhomogeneity) is anticipated along the Ni/4H-SiC Schottky junction [4, 10].

The conventional Richardson's plot $ln(J_s/T^2)$ vs. q/kT for Ni/4H-SiC SBD is constructed in figure 3(b), as per the expression derived from J_s equation [1]

$$\ln\left(\frac{J_s}{T^2}\right) = -\frac{q}{kT}\Phi_{\text{eff}} + \ln\left(A^*\right). \tag{4}$$

The slope of the conventional Richardson's plot yields the effective SBH of 1.06 eV, which is much lower than the SBH value (1.31 eV) at 300 K, as similar to the observations of Roccaforte *et al* [10]. This reiterates the non-ideal inhomogeneous Schottky barrier behavior at the Ni/4H-SiC interface. It should be noted that the conventional Richardson analysis is only applicable for ideal cases [1–3] (temperature-independent SBH and n) and near-ideal SBDs (SBH decreases and n increases with temperature). For the non-ideal Ni/4H-SiC SBD, modified Richardson's plot is created by including the ideality factor temperature dependence in the equation (4), based on the work of Roccaforte *et al* [10]

$$\ln\left(\frac{J_s}{T^2}\right) = -\frac{q}{nkT}\Phi_{\text{eff}} + \ln\left(A^*\right). \tag{5}$$

The effective SBH ($\Phi_{eff} = 1.35$ eV) is determined from the slope of $ln(J_s/T^2)$ vs. q/nkT plot in figure 3(b). This Φ_{eff} lies between the room temperature and the high-temperature SBH values (1.31–1.43 eV), supporting the literature report [10].

In general, the low SBH (1.31–1.43 eV) patches are only identified from the *I*–*V* characteristics [10]. Tung's model [18] suggests that a typical non-ideal Schottky interface contains a spatially-homogeneous large barrier (Φ_B^0), which is calculated from the relation between SBH and n [10]. Figure 4(a) plots the measured SBH vs. n for the Ni/4H-SiC SBDs; The linear interpolation of the plot at $n = 1$ yields $\Phi_{B-Ni}^0 = 1.66$ eV.

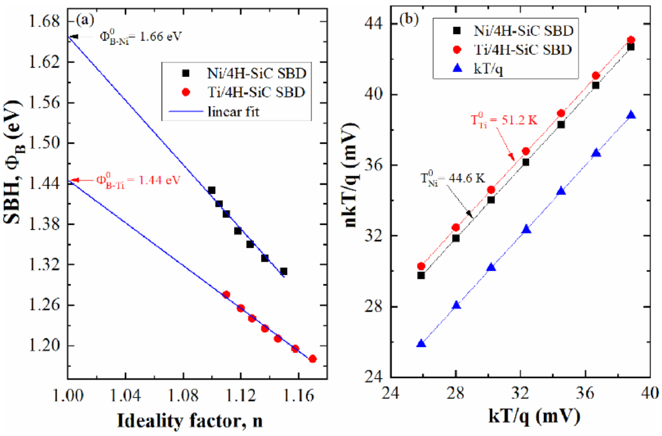

Figure 4. (a) SBH (Φ_B) vs. n is plotted for Ni/4H-SiC and Ti/4H-SiC SBDs (b) T_0 anomaly ($n = 1 + T_0/T$) is computed from nkT/q vs. kT/q plot for Ni/4H-SiC and Ti/4H-SiC SBDs.

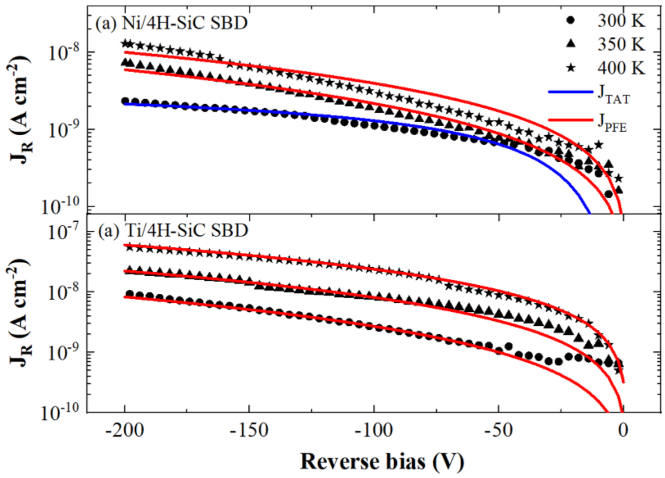

Figure 5. Reverse current transport mechanisms (TAT and PFE) in (a) Ni/4H-SiC SBD, and (b) Ti/4H-SiC SBD are identified by fitting the experimental J_R–V_R data.

The temperature dependence of n for the inhomogeneous SBD is described by $n = 1 + T_0/T$ [3, 10]. T_0 predicts the temperature dependence of n over a wide temperature range and is referred to as 'T_0 anomaly' [10]. Hence, a high T_0 corresponds to a highly inhomogeneous barrier distributed along the metal/semiconductor interface. In ideal SBDs, n must be unity even after increasing the temperature, as shown in kT/q vs. kT/q reference curve in figure 4(b). Due to the temperature dependency, nkT/q vs. kT/q plot occurs in parallel with the ideal curve [10]. T_0 anomaly of 44.6 K is extracted for the Ni/4H-SiC SBDs through the linear regression of the nkT/q vs. kT/q plot.

The carrier transport processes responsible for the reverse current density-voltage-temperature (J_R–V_R–T) characteristics of Ni/4H-SiC SBDs are plotted in figure 5(a). It is found that the trap-assisted tunneling (J_{TAT}) model nearly tracks J_R–V_R at 300 K, as estimated by the equation [13, 14]

$$J_{\mathrm{TAT}} = A_{\mathrm{TAT}} \exp\left(-\frac{4\sqrt{2m_n}(q\varphi_t)^{3/2}}{3q\hbar E_{\mathrm{m}}}\right) \tag{6}$$

where A_{TAT} is the TAT model fitting parameter, $q\phi_t$ is the energy location of the trap at E_C—E_T, m_n is the electron effective mass, $\hbar$ is the reduced Plank's constant, and E_m is the maximum electric field at the Schottky junction. It is accounted that the TAT tunneling takes place via an electron trap at E_C—0.65 eV. In fact, this trap $Z_{1/2}$ is detected in the Ni/4H-SiC SBDs by TSCAP (discussed later). Hence, the selected trap energy at E_C—0.65 eV in the TAT model has a physical significance. At higher temperatures, J_R–V_R properties of the Ni/H-SiC SBDs are fitted by the Poole-Frenkel emission (PFE) model (J_{PFE}) [1, 9]

$$J_{\mathrm{PFE}} = A_{\mathrm{PFE}} E_{\mathrm{m}} \exp\left(\frac{-q\left(\varphi_t - \sqrt{qE_{\mathrm{m}}/\pi\varepsilon_s}\right)}{kT}\right) \tag{7}$$

where A_{PFE} is the PFE model fitting parameter, and ε_s is the dielectric constant of the semiconductor. The PFE model

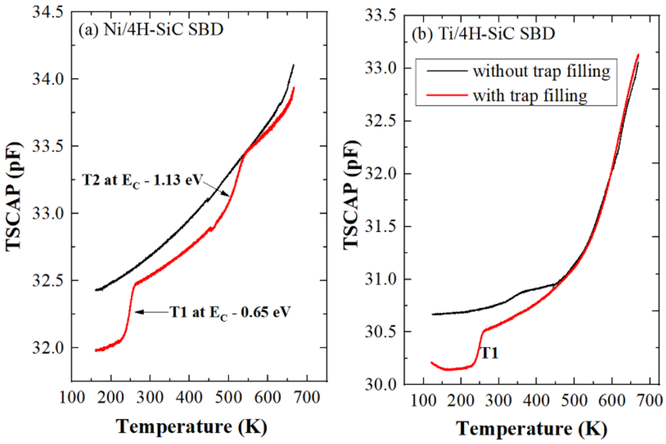

Figure 6. Measured TSCAP of (a) Ni/4H-SiC SBD, (b) Ti/4H-SiC SBD shows two traps at E_C—0.65 eV (T1) and E_C—1.13 eV (T2).

(with the same trap at E_C—0.65 eV) has agreed well with the experimental J_R–V_R data at 350 K and 400 K, as seen in figure 5(a). So, it is stated that the trap-related carrier transport models such as TAT and PFE primarily decide the J_R–V_R–T properties of Ni/4H-SiC SBDs.

The measured TSCAP spectroscopy for Ni/4H-SiC SBD is plotted in figure 6(a). It is noticed that the depletion capacitance of the SBD increases with the temperature due to the reduction in V_{bi} [1]. Relative to the without trap filling case, two increasing capacitance steps (T1 and T2) are noticed in the TSCAP spectrum obtained upon the trap filling at T_f. The electron emission from a trap at E_C—E_T (majority carrier trap in n-type semiconductor) is responsible for the rising capacitance steps in figure 6(a) [19, 20]. The mid-step temperature ($T_{1/2}$) is extracted for each TSCAP step, and the trap activation energy (E_a) is computed by [19, 20]

$$E_{\mathrm{a}} = kT_{1/2} \ln\left[\frac{vkT^2_{1/2}}{q\left(E_{\mathrm{T}} + 2kT_{1/2}\right)}\right] \tag{8}$$

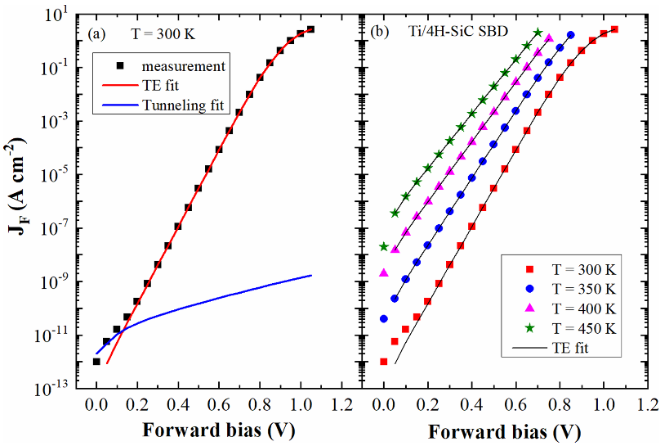

Figure 7. (a) TE and tunneling current components in J_F–V_F properties of Ti/4H-SiC SBD at 300 K. (b) J_F–V_F at different temperatures (300 K–450 K) is fitted with the TE model.

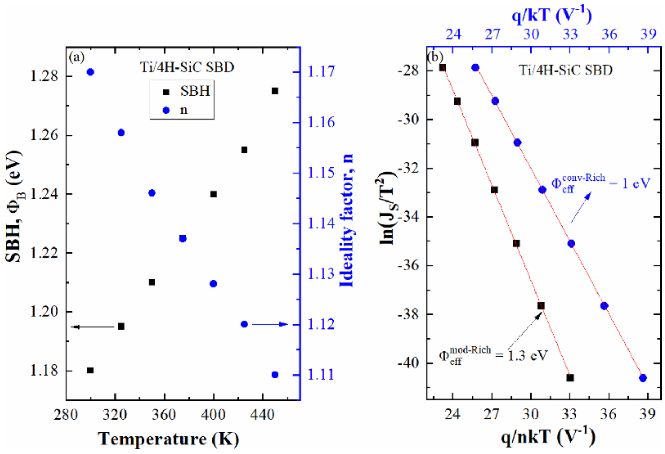

Figure 8. (a) Temperature dependent (300–450 K) SBH and n values for Ti/4H-SiC SBDs. (b) The conventional and modified Richardson plots for the Ti/4H-SiC SBDs.

where v is the escape frequency factor ($v = \sigma_n\ N_C\ v_{th}$), σ_n is the trap capture cross-section, N_C is the effective density of states in the conduction band, and v_{th} is the thermal velocity. The energy level of traps $T1$ and $T2$ is found to be E_C—0.65 eV, and E_C—1.13 eV, with $\sigma_n = 5 \times 10^{-16}$ cm^2 ($T1$) and 3×10^{-18} cm^2 ($T2$). The trap concentration (N_T) for $T1$ ($\sim 10^{13}$ cm^{-3}) and $T2$ (1.3×10^{13} cm^{-3}) is estimated by the following equation [19, 20]

$$N_T \approx 2N_D \frac{\Delta C}{C_R} \tag{9}$$

where N_D is the epilayer doping concentration, ΔC is the magnitude of the TSCAP signal step, i.e. C_2—C_1, and C_R is the reverse bias depletion capacitance. The electron trap $T1$ at E_C—0.65 eV might be created due to the omnipresent $Z_{1/2}$ defect in the n-type 4H-SiC [6]. The other trap $T2$ at E_C—1.13 eV may be related to the EH5 defect state [6, 21].

3.2. Ti/4H-SiC SBDs

Figure 7(a) depicts the J_F–V_F characteristics of Ti/4H-SiC SBD at 300 K. The fitting analysis shows that the tunneling is responsible for J_F at low $V_F < 0.1$; after that, the standard TE fully governs J_F. The SBH and n of the Ti/4H-SiC are computed as 1.18 eV, and 1.17, respectively. Compared to the Ni/4H-SiC SBDs, forward J_{TU}, and V_{ON} at 10 mA cm^{-2} (0.76 V at 300 K) are lesser in the Ti/4H-SiC SBDs, which may be due to the relatively smaller SBH. The J_F–V_F–T characteristics of the Ti/4H-SiC SBDs also follow the TE theory, as observed in figure 7(b). Similar to Ni/4H-SiC SBDs, V_{ON} at 10 mA cm^{-2} decreases with the temperature (0.66 V at 350 K, and 0.48 V at 450 K) because of the reduction in V_{bi}.

Alike Ni/4H-SiC SBDs, SBH of the Ti/4H-SiC SBD increases with the temperature (1.18 eV at 300 K, 1.225 eV at 375 K, and 1.275 eV at 450 K), as noted from figure 8(a). Likewise, n decreases with the temperature (1.17 at 300 K, 1.137 at 375 K, and 1.11 at 450 K), specifying the barrier inhomogeneity at the Ti/4H-SiC interface [4, 10]. The effective SBH (1 eV) identified from the conventional Richardson plot is lower than the value attained at 300 K, as perceived from figure 8(b). Therefore, the effective SBH of $\Phi_{eff} = 1.3$ eV is calculated from the modified Richardson plot shown in figure 8(b). The effective SBH (1.3 eV) is higher than the theoretical SBH (1.23 eV) estimated based on the Schottky-Mott theory equation [1–3], by taking the electron affinity of 4H-SiC as 3.1 eV and the Ti work function as 4.33 eV. This observation reveals that the SBH of the Ti/4H-SiC SBD is decided by the Fermi level pinning effect induced by the surface and interface states [1–3]. Indeed, the Fermi level pinning has positively impacted the Ti/4H-SiC interface by increasing the SBH more than the theoretical prediction. The spatially-uniform large barrier ($\Phi^0_{B-Ti} = 1.44$ eV) is determined from SBH vs. n plot in figure 4(a). T_0 anomaly (51.2 K) for the Ti/4H-SiC SBDs is computed from nkT/q vs. kT/q plot in figure 4(b). T_0 value is slightly higher than the Ni/4H-SiC SBDs, signifying that Ti/4H-SiC interface has a high degree of barrier inhomogeneity [10].

Figure 5(b) illustrates that the PFE model (J_{PFE}) fairly predicts J_R–V_R of Ti/4H-SiC SBDs at different temperatures (300 K–400 K). The TSCAP in figure 6(b) reveals only a single trap T1 at E_C—0.65 eV ($Z_{1/2}$) in Ti/4H-SiC SBDs, so the deep-level trap T2 is not detected. Overall, the Ti/4H-SiC SBDs have shown promising results such as reasonably high SBH of 1.18 eV, low V_{ON}, and low J_R (on par with Ni/4H-SiC SBDs), for rectifier applications.

3.3. Vertical Ni/GaN SBDs

The J_F–V_F–T characteristics of vertical Ni/GaN SBDs are plotted in figure 9(a). It is found that the standard J_{TE} controls the forward-biased Ni/GaN SBDs over the temperature range of 293 K–393 K. Thus, the forward J_{TU} is negligible in the

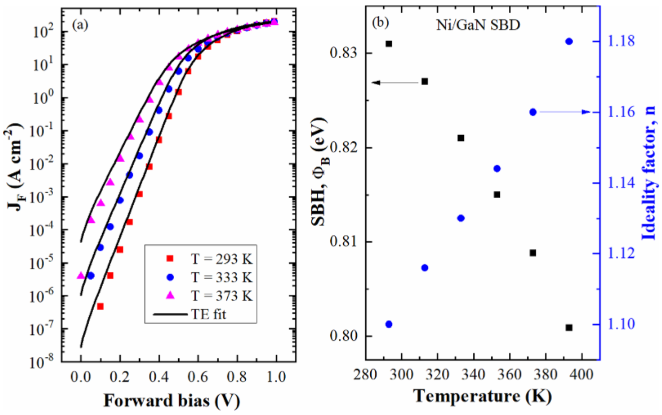

Figure 9. (a) J_F–V_F–T of the vertical Ni/GaN SBDs are fitted by the TE model. (b) Changes in the SBH and n of the Ni/GaN SBD in the temperature range of 293 K–393 K.

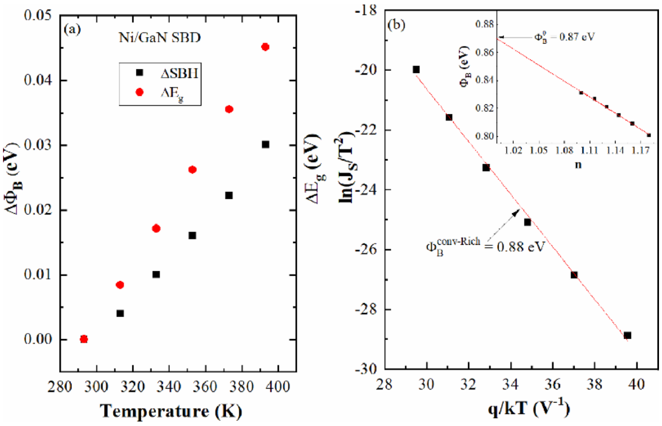

Figure 10. (a) Correlation of temperature-induced changes in SBH ($\Delta\Phi_B$) and bandgap of GaN (ΔE_g). (b) Conventional Richardson's plot for Ni/GaN SBDs and the inset shows the SBH vs. n plot.

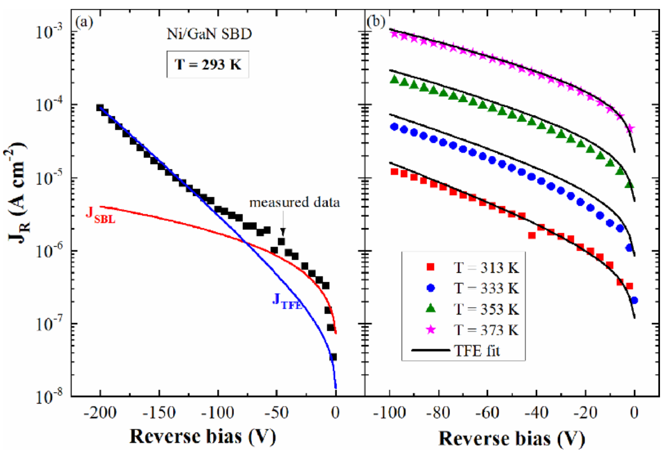

Figure 11. (a) The SBL and TFE components in the reverse current density of the Ni/GaN SBDs at 293 K. (b) The TFE model fairly predicts J_R–V_R in the temperature range of 313–373 K.

Ni/GaN SBDs. The SBH and n at 293 K are found to be 0.83 eV, and 1.1, respectively. Due to the high $\chi = 4$ eV, a low SBH value is obtained for the Ni/GaN SBDs, in comparison with the 4H-SiC SBDs. V_{ON} (0.36 V at 10 mA cm^{-2}) is lower than in 4H-SiC SBDs. As anticipated, V_{ON} at 10 mA cm^{-2} decreases with the temperature due to the decreased V_{bi}. Conversely, V_{ON} at 180 A cm^{-2} increases with the temperature (the augmented series resistance effect is not visible in the semi-log J_F–V_F plot) due to the mobility degradation [5].

It is shown in figure 9(b) that the SBH decreases with the increasing temperature (0.83 eV at 293 K, 0.815 eV at 353 K, and 0.8 eV at 393 K), as opposed to the 4H-SiC SBDs. The temperature-caused reduction in SBH is correlated with the bandgap narrowing effect in the GaN, as per the equation [1]

$$E_g(T) \approx E_g(0) - \frac{\alpha T^2}{T+\beta} \tag{10}$$

where E_g (T) is the temperature dependency of the bandgap, E_g (0) is the bandgap of the semiconductor at 0 K, α and β are the material-dependent parameters. The temperature-induced changes in the SBH ($\Delta\Phi_B$) and the bandgap of GaN (ΔE_g) are compared in figure 10(a). The parameter values of E_g $(0) = 3.47$ eV, $\alpha = 9.09 \times 10^{-4}$ eV/K, and $\beta = 836$ K are chosen based on the Sentaurus TCAD material parameter files [22]. The temperature-induced variations in $\Delta\Phi_B$ and ΔE_g follow a similar trend, signifying that these physical processes (parameter variations) are interrelated, although the values slightly differ. Accordingly, the bandgap narrowing effect of GaN is considered the prime reason for the reduction in the SBH upon increasing the temperature. The ideality factor of the Ni/GaN SBD increases with the temperature (1.1 at 293 K, 1.144 at 353 K, and 1.18 at 393 K), possibly due to the notable increase in the forward TFE current density [1, 3].

The effective SBH (0.88 eV) for the Ni/GaN SBD is determined from the conventional Richardson plot in figure 10(b). As the temperature dependence of the SBH and ideality factor obeys the nearly-ideal behavior, modified Richardson plot and T_0 anomaly analysis are not required for the GaN SBDs. In fact, the modified Richardson plot underestimates the effective SBH (0.81 eV), as n reduces with the temperature. Φ_B^0 for the Ni/GaN SBD is extracted as 0.87 eV, from the SBH vs. n plot [10] in the inset of figure 10(b). It is noted that Φ_B^0 value (0.87 eV) closely resembles the effective SBH (0.88 eV) of the Ni/GaN SBDs.

Figure 11(a) depicts J_R–V_R characteristics of the Ni/GaN SBDs at 293 K. It is perceived that the Schottky barrier lowering effect (SBL) contributes to J_R up to -50 V; beyond that voltage, TFE entirely governs the J_R–V_R properties. The increase in J_R due to the SBL effect (J_{SBL}) is expressed by [1–3, 14]

$$J_{SBL} = A^* T^2 \exp\left(-\frac{q(\Phi_B - \Delta\varphi)}{kT}\right) \tag{11}$$

$$\Delta\varphi = \sqrt{\frac{qE_m}{4\pi\varepsilon_s}} \tag{12}$$

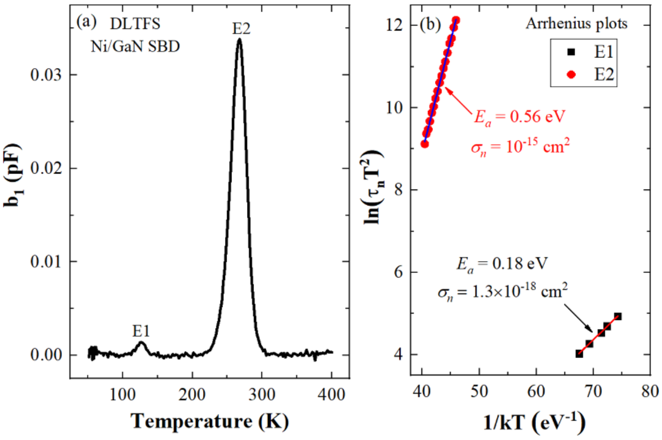

Figure 12. (a) Measured DLTFS for Ni/GaN SBD (first order Fourier sine coefficient b_1 used). (b) Arrhenius plots for traps E1 and E2.

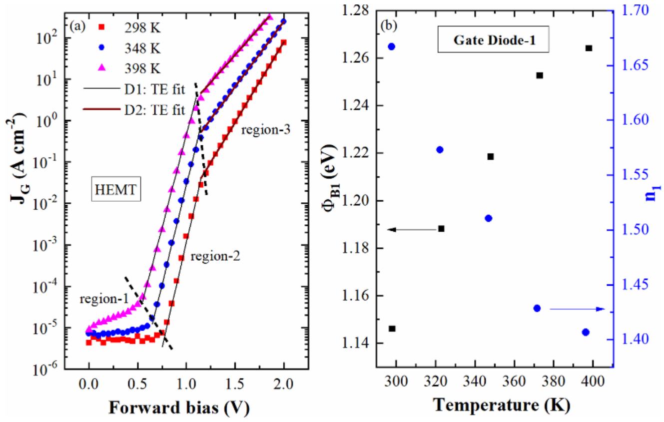

Figure 13. (a) J_G–V_G characteristics of AlGaN/GaN HEMT show three different regions of operation during forward bias. (b) Temperature dependence of Φ_{B1} and n_1 for the gate diode-1.

where $\Delta\phi$ is the SBL-induced reduction in SBH. The TFE model (J_{TFE}) is symbolized based on the Sze's equation [1]

$$J_{TFE} = \frac{A^* T}{k}\sqrt{\pi E_{00}\, q\left[V_R + \frac{\Phi_B}{\cosh^2\left(E_{00}/kT\right)}\right]} \times \exp\left(\frac{-q\Phi_B}{E_0}\right)\exp\left(\frac{qV_R}{\varepsilon'}\right) \quad (13)$$

$$\varepsilon' = \frac{E_{00}}{\left(E_{00}/kT\right) - \tanh\left(E_{00}/kT\right)}. \quad (14)$$

The J_R–V_R–T characteristics (from 293 K to 373 K) are fairly predicted by the TFE model, as illustrated in figure 11(b). These observations reveal that the TFE is the primary current transport in the reverse-biased Ni/GaN SBDs. In literature, Ren *et al* [14] demonstrated nearly-ideal *I*–*V* characteristics for Ni/GaN SBD with SBH = 0.97 eV, and n = 1.04. The SBH and n values for Au/GaN SBDs are reported [23, 24] in the range of 0.83–0.9 eV, and 1.06–1.15, respectively. The current results suggest that the studied Ni/GaN SBDs used exhibit quasi-ideal characteristics, such as SBH = 0.83 eV, n = 1.1, and typical temperature dependence of SBH and n.

The DLTFS represented in first-order Fourier sine coefficient b_1 for the Ni/GaN SBD is shown in figure 12(a). Two positive DLTFS peaks E1 and E2 are produced due to the electron emission from the trap at E_C—E_T (based on our DLTFS measurement setup) [25]. The Arrhenius plots for E1 and E2 are made in figure 12(b). E_a, and σ_n of the traps are computed from the slope and intercept of the Arrhenius plot as per the following expression [26]

$$\ln\left(\tau_n T^2\right) = \frac{E_a}{kT} - \ln\left(\frac{\sigma_n N_C v_{th}}{g T^2}\right) \quad (15)$$

The b_1 signal magnitude (ΔC) for E1 and E2 is extracted [23] and N_T for the traps is estimated using the equation (9). Accordingly, trap signatures such as E_a, σ_n, and N_T are determined for E1 (E_C—0.18 eV, 1.3 × 10^{-18} cm^2, 4 × 10^{13} cm^{-3}) and E2 (E_C—0.56 eV, 10^{-15} cm^2, 8 × 10^{14} cm^{-3}). The shallow electron trap E1 at E_C—0.18 eV is ascribed to the nitrogen-vacancy (V_N) defect in the GaN epilayer [27]. Other electron trap E2 at E_C—0.56 eV may be related to the nitrogen-antisite (N_{Ga}) intrinsic defect in the GaN layers [28].

3.4. GaN/AlGaN/GaN HEMT

Figure 13(a) shows the forward J_G-V_G characteristics (for V_{DS} = 0 V) of the AlGaN/GaN HEMT at 298 K, 348 K, and 398 K. The fitting analysis reveals the three different regions of operation in the forward J_G–V_G–T properties. The forward current density is low and nearly unchanged with the applied voltage in region-1 (V_G < 0.7 V), so the saturation current density is the only possible mechanism in this region. Thereafter, two linear regions are observed in figure 13(a) with dissimilar slopes, revealing the presence of two non-identical SBHs at metal/GaN/AlGaN/GaN interface [29, 30]. Note that, the series resistance effect produces a linear region in the linearly scaled J_F–V_F characteristics at higher current densities [1, 8], but it does not induce a linear segment in the semilog J_F–V_F and $ln(J_F)$ vs. V_F plots. This point confirms that metal/GaN/AlGaN/GaN system has the two-diode model properties, as reported by Chen *et al* [29] and Greco *et al* [30].

In the two-diode model [29, 30], the first diode (SBH-1) corresponds to the regular metal/GaN Schottky barrier junction; while, the second diode (SBH-2) forms due to the energy difference between the AlGaN conduction band edge and the Fermi level of the AlGaN/GaN heterointerface, as illustrated in figure 14(a). Using the TE model, the SBH at 298 K for the first and second diodes of the HEMT gate is calculated as 1.15 eV (Φ_{B1}), and 0.72 eV (Φ_{B2}), respectively. Theoretical

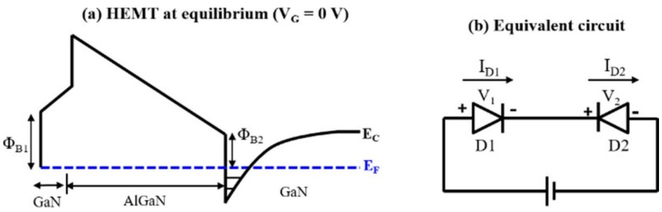

Figure 14. (a) Schematic conduction band diagram at equilibrium shows SBH-1 at metal/semiconductor interface and SBH-2 at the AlGaN/GaN heterointerface. (b) The equivalent circuit for the two diode model associated with the metal/GaN/AlGaN/GaN interface.

SBH of 1.15 eV is computed for the Ni/GaN cap Schottky barrier gate diode-1, by taking $\chi_{\mathrm{GaN}} = 4$ eV and $\phi_{\mathrm{m\text{-}Ni}} = 5.15$ eV. Similarly, the ideality factor for the gate diode-1 and 2 is calculated 1.67 (n_1), and 4.36 (n_2). Since the gate diode-2 is associated with the unusual AlGaN/GaN interface, a largely deviated ideality factor of 4.36 (n_2) is attained.

The two-diode model of Chen *et al* [29] and Greco *et al* [30] describes that the diodes are serially connected in a back-to-back arrangement at the metal/GaN/AlGaN/GaN interface. The equivalent circuit for the two-diode model of the HEMT gate structure is visualized in figure 14(b). The applied V_{G} to the metal/GaN/AlGaN/GaN system may equal to the sum of the voltage drop across the diode-1 and diode-2 (i.e. $V_{\mathrm{G}} = V_1 + V_2$) [27, 28]. For 0.7 V $< V_{\mathrm{G}} <$ 1.25 V, the gate diode-1 is forward-biased due to the applied voltage drop V_1. The diode-1 current density (J_{GD1}) in region-2 can be represented by the TE model equation ($V_{\mathrm{G}} \gg kT/q$), neglecting the series resistance effect [29, 30]

$$J_{\mathrm{GD1}} = A^* T^2 \exp\left(\frac{-q\Phi_{\mathrm{B1}}}{kT}\right) \exp\left(\frac{qV_1}{n_1 kT}\right) = J_{\mathrm{s1}} \exp\left(\frac{qV_1}{n_1 kT}\right) \tag{16}$$

where J_{s1} is the saturation current density for the diode-1, and V_1 is the voltage drop across the diode-1. In region-3, the applied V_{G} (>1.25 V) may drop across the diode-2, as a result, the diode-2 is reverse biased. It is considered that the reverse current density of the gate diode-2 (J_{GD2}) is roughly equal to the reverse saturation current density [29, 30]

$$J_{\mathrm{GD2}} \approx A^* T^2 \exp\left(\frac{-q\Phi_{\mathrm{B2}(V_2)}}{kT}\right). \tag{17}$$

If the diode-2 is reverse-biased, the resulting current (I_{D2}) is directed from the cathode to the anode terminal of the diode-2. Consequently, the diode-2 current direction (I_{D2}) is similar to that of I_{D1}. Hence, a negative sign is not required for the diode-2 current. Since V_{G} changes the Fermi level position and modulates the 2DEG density at the AlGaN/GaN heterointerface, the SBH-2 (Φ_{B2}) becomes a bias-dependent. It is worth noting that the applied gate voltage does not modify the SBH-1 at the metal/GaN interface [1]. The SBH-2 voltage dependence, $\Phi_{B2(V_2)}$, is symbolized as per the first-order Taylor series expansion [29, 30]

$$\Phi_{\mathrm{B2}(V_2)} = \Phi_{\mathrm{B2}(0)} - \left(\frac{\partial \Phi_{\mathrm{B2}}}{\partial V_2}\right) V_2 = \Phi_{\mathrm{B2}(0)} - \left(\frac{1}{n_2}\right) V_2 \tag{18}$$

where $\Phi_{\mathrm{B2}(0)}$ is the zero-bias SBH for the diode-2, $\partial\Phi_{\mathrm{B2}}/\partial V_2$ defines the bias voltage dependency of the SBH-2, and V_2 is the voltage drop across the diode-2. The gate voltage-induced change in the SBH-2 ($\partial\Phi_{\mathrm{B2}}/\partial V_2$) is related to the reciprocal of the diode-2 ideality factor ($1/n_2$). Accordingly, it is presumed that the SBH-2 variation is small compared to the V_2 change, thereby resulting in a high n value ($n_2 = 4.36$) for the diode-2. After substituting $\Phi_{\mathrm{B2}}(V_2)$ into equation (17), J_{GD2} expression is rewritten as [29, 30]

$$J_{\mathrm{GD2}} = A^* T^2 \exp\left(\frac{-q\Phi_{\mathrm{B2}(0)}}{kT}\right) \exp\left(\frac{qV_2}{n_2 kT}\right) = J_{\mathrm{s2}} \exp\left(\frac{qV_2}{n_2 kT}\right). \tag{19}$$

The above equation is valid only during the reverse bias operation of the diode-2; however this expression is identical to the forward-biased diode-1 equation (TE model) [29, 30]. The diode-2 current also flows from the higher potential to the lower potential of the bias supply, as represented in figure 14(b). Thus, the forward J_{G}–V_{G} properties of the HEMT gate can be modeled using the TE model with two different SBHs.

Since the gate diode-1 is related to the standard metal/GaN Schottky interface, the temperature dependence of the SBH-1 (Φ_{B1}) and n_1 are discussed first. It is perceived in figure 13(b) that SBH-1 increases and n_1 decreases with the temperature, indicating the Schottky barrier inhomogeneity at the Ni/GaN cap interface. As anticipated for the non-ideal Schottky junction [10], the conventional Richardson plot undervalues (0.8 eV) the effective SBH. Furthermore, figure 15(a) specifies that the modified Richardson analysis yields an unrealistic effective SBH (3 eV) for the metal/GaN Schottky junction. It is found that the temperature-induced changes in n_1 of the diode-1 do not follow the T_0 anomaly expression. From the SBH-1 vs. n_1 plot (not shown), the spatially-uniform high barrier for the metal/GaN cap interface is calculated as 1.45 eV, which is much higher than the theoretical SBH (1.15 eV) projected by the Schottky-Mott equation. Figure 15(b) plots the SBH-2 (Φ_{B2}) and n_2 variations with the temperature for the gate diode-2. SBH-2 slightly decreases and n_2 increases with the temperature. The heterojunction Fermi level may move downwards as the temperature increases [1]. In this condition, the SBH-2 should increase with the temperature; a contradictory nature is observed in figure 15(b). In addition, the diode-2 is associated with the peculiar AlGaN/GaN interface system (not a typical metal/semiconductor junction); hence diode-2 parameters are not further investigated.

The reverse J_{G}–V_{G} characteristics of the HEMT gate diode at different temperatures are plotted in figures 16(a) and (b).

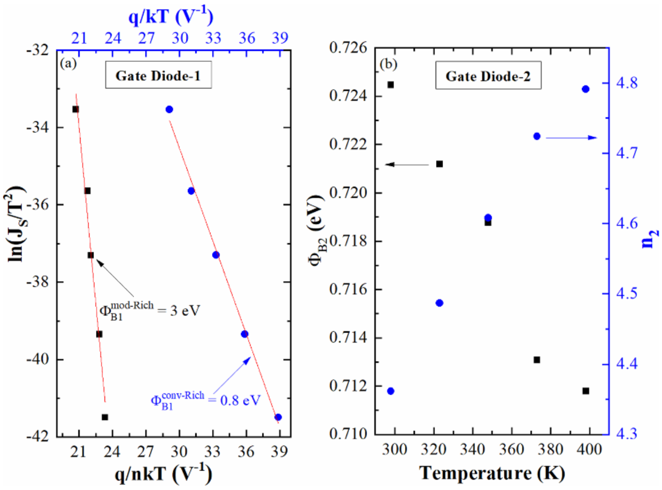

Figure 15. (a) The conventional and modified Richardson's plots for the Schottky gate diode-1. (b) The SBH-2 (Φ_{B2}) and n_2 variations with the temperature for the gate diode-2.

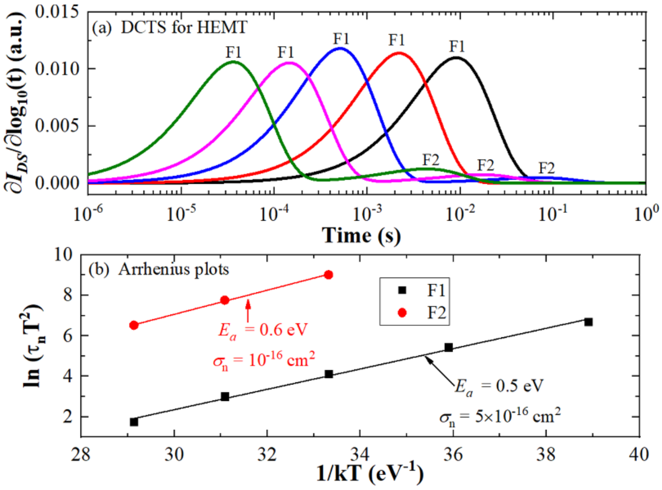

Figure 17. (a) Derivative of DCTS of AlGaN/GaN HEMT shows two traps F1 and F2. (b) Arrhenius plots for F1 and F2.

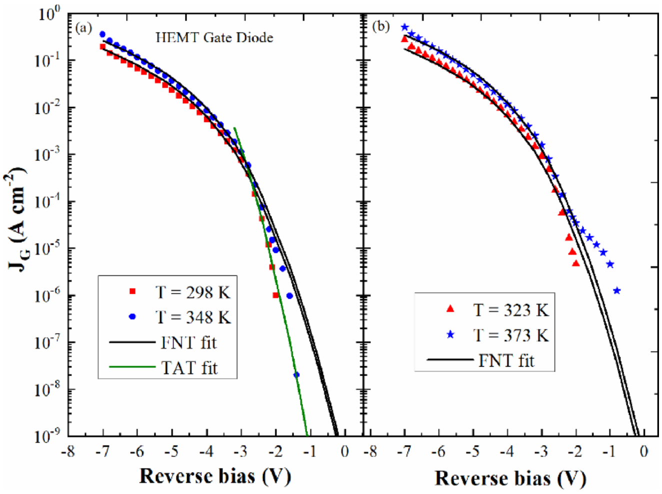

Figure 16. (a) The reverse J_G–V_G characteristics of Schottky gate diode at two different temperatures of 298 K and 348 K. (b) The reverse J_G–V_G is fitted with the FNT model at 323 K and 373 K.

For low reverse voltages ($V_G > -1$ V), the leakage current sign is obtained in another direction (semilog plot ignores negative values), possibly due to the instrument noise (current is very low). In the intermediate range (-2 V $< V_G < -1$ V), J_G–V_G properties are fitted with the TAT model, as seen in figure 16(a). However, beyond that voltage ($V_G < -2$ V), the J_{TAT} overestimates the gate leakage current density. So, the reverse J_G–V_G fitting is accomplished by Fowler-Nordheim tunneling (FNT) current density equation (J_{FNT}) [1, 9]

$$J_{FNT} = A_{FNT} E_m^2 \exp\left(-\frac{-4\sqrt{2m_n}(q\Phi_B)^{3/2}}{3q\hbar E_m}\right) \quad (20)$$

where A_{FNT} is the FNT model fitting parameter. The electric field at the AlGaN/GaN heterojunction computed from the TCAD simulations [22] is used in TAT and FNT models.

Figures 16(a) and (b) the FNT model reasonably predicts the reverse J_G for $V_G < -2$ V over the wide temperature range of 293–373 K. Therefore, it is considered the FNL transport plays a significant role in deciding the reverse gate current properties of the GaN/AlGaN/GaN HEMT.

Two distinct positive peaks F1 and F2 are identified in the derivative DCTS for AlGaN/GaN HEMT in figure 17(a). Our earlier simulation studies [24] suggest that the electron trapping in the GaN buffer layer can induce a positive DCTS peak. The emission time constant (τ_n) decreases with temperature, and its temperature dependency follows the Arrhenius equation (15). Hence, E_a and σ_n of the traps F1 (E_C—0.5 eV, 5×10^{-16} cm^2) and F2 (E_C—0.6 eV, 10^{-16} cm^2) are identified from the Arrhenius plots in figure 17(b). Based on our earlier findings and literature reports, the traps F1 at E_C—0.5 eV and F2 at E_C—0.6 eV are attributed to the Fe-doping-related acceptor states in the GaN buffer region [24].

The electrical parameters (SBH, n, V_{ON} at 10 mA cm^{-2}, Φ_{eff}, Φ_B^0, T_0 anomaly for 4H-SiC SBDs), dominant forward J_F and reverse J_R transport models, trap signatures (E_T, σ_n, N_T) for Ni/4H-SiC SBD, Ti/4H-SiC SBD, Ni/GaN SBD, metal/GaN/AlGaN/GaN HEMT gate diode-1 and diode-2 are summarized in table 1.

4. Conclusion

The forward and reverse current transport models, temperature dependence of SBH and n, T_0 anomaly for non-ideal diodes, effective SBH, and trap parameters for Ni/4H-SiC, Ti/4H-SiC, Ni/GaN SBDs, and Schottky gate diode of AlGaN/GaN HEMT are presented. Both 4H-SiC SBDs demonstrated excellent electrical properties, high SBH (>1 eV), low J_R ($<10^{-8}$ A cm^{-2} at -200 V), low V_{ON} (<0.9 V at 10 mA cm^{-2}), and $V_{BR} < -200$ V for rectifier applications. Two deep-level traps at E_C—0.65 eV and E_C—1.13 eV are detected in the 4H-SiC SBDs. The Ni/GaN SBDs exhibited quasi-ideal characteristics with $n = 1.1$, SBH of 0.83 eV, and

Table 1. Electrical parameters, dominant forward J_F and reverse J_R models, and trap signatures for various SBD devices.

Parameter	Ni/4H-SiC SBD	Ti/4H-SiC SBD	Ni/GaN SBD	HEMT gate diode-1	HEMT gate diode-2
SBH (eV)	1.31 (at 300 K)	1.18 (at 300 K)	0.83 (at 293 K)	1.15 (at 298 K)	0.72 (at 298 K)
n	1.15 (at 300 K)	1.17 (at 300 K)	1.1 (at 293 K)	1.67 (at 298 K)	4.36 (at 298 K)
V_{ON} at 10 mA cm^{-2} (V)	0.88 (at 300 K)	0.76 (at 300 K)	0.36 (at 293 K)	1.1 (at 298 K) from forward J_G–V_G	
Φ_{eff} (eV)	1.35	1.3	0.88	[a]	[a]
Φ_B^0 (eV)	1.66	1.44	0.87	[a]	[a]
T_0 anomaly (K)	44.6	51.2	[a]	[a]	[a]
Dominant J_F model	TE (all T)	TE (all T)	TE (all T)	TE (all T)	TE (all T)
Dominant J_R model	TAT at 300 K PFE for $T \geqslant 350$ K	PFE for 300 K $\leqslant T \leqslant$ 400 K	TFE for 293 K $\leqslant T \leqslant$ 373 K	FNL for 298 K $\leqslant T \leqslant$ 398 K	
Trap-1 signatures (E_T, σ_n, N_T)	T1 at E_C—0.65 eV, $\sim 5 \times 10^{-16}$ cm^2, $\sim 10^{13}$ cm^{-3}	T1 at E_C—0.65 eV, $\sim 5 \times 10^{-16}$ cm^2, $\sim 10^{13}$ cm^{-3}	E1 at E_C—0.18 eV, 1.3×10^{-18} cm^2, 4×10^{13} cm^{-3}	F1 at E_C—0.5 eV, $\sigma_n = 5 \times 10^{-16}$ cm^2	
Trap-2 signatures (E_T, σ_n, N_T)	T2 at E_C—1.13 eV, $\sim 3 \times 10^{-18}$ cm^2, $\sim 1.3 \times 10^{13}$ cm^{-3}	T2 is not detected	E2 at E_C—0.56 eV, 10^{-15} cm^2, 8×10^{14} cm^{-3}	F2 at E_C—0.6 eV, $\sigma_n = 10^{-16}$ cm^2	

[a] Not applicable for these devices.

two electron traps at E_C—0.18 eV and E_C—0.56 eV are identified. The Schottky gate of the HEMT has shown a two-diode model behavior, such that, diode-1 corresponds to the regular metal/GaN Schottky barrier junction; while diode-2 forms at the unusual AlGaN/GaN heterointerface due to the energy difference between the Fermi level and AlGaN conduction band. The Fe-doping-related traps at E_C—0.5 eV and E_C—0.6 eV are determined in the HEMTs by the DCTS technique.

Data availability statement

All data that support the findings of this study are included within the article (and any supplementary files).

ORCID iDs

N V L Narasimha Murty https://orcid.org/0000-0003-2253-5383
Hassan Maher https://orcid.org/0000-0002-3827-2517
P Vigneshwara Raja https://orcid.org/0000-0002-9599-2000

References

[1] Sze S M and Ng N N 2007 *Physics of Semiconductor Devices* (Wiley)
[2] Rhoderick E H 1982 Metal-semiconductor contacts *IEE Proc.* **129** 1
[3] Tyagi M S 1984 *Physics of Schottky Barrier Junctions, Metal-Semiconductor Schottky Barrier Junctions and Their Applications* (Plenum Press)
[4] Werner J H and Güttler H H 1991 Barrier inhomogeneities at Schottky contacts *J. Appl. Phys.* **69** 1522
[5] Baliga A J 2019 *Fundamentals of Power Semiconductor Devices* (Springer)
[6] Kimoto T and Cooper J A 2014 *Fundamentals of Silicon Carbide Technology: Growth, Characterization, Devices, and Applications* (Wiley)
[7] Onsemi silicon carbide Schottky diode *NDC25170A Datasheet* (available at: www.onsemi.com/pdf/datasheet/ndc25170a-d.pdf)
[8] Meneghini M *et al* 2021 GaN-based power devices: physics, reliability, and perspectives *J. Appl. Phys.* **130** 181101
[9] Turuvekere S, Karumuri N, Rahman A A, Bhattacharya A, DasGupta A and DasGupta N 2013 Gate leakage mechanisms in AlGaN/GaN and AlInN/GaN HEMTs: comparison and modelling *IEEE Trans. Electron Devices* **60** 3157
[10] Roccaforte F, Giannazzo F, Alberti A, Spera M, Cannas M, Cora I, Pécz B, Iucolano F and Greco G 2019 Barrier inhomogeneity in vertical Schottky diodes on free standing gallium nitride *Mater. Sci. Semicond. Process.* **94** 164
[11] Maeda T, Okada M, Ueno M, Yamamoto Y, Kimoto T, Horita M and Suda J 2017 Temperature dependence of barrier height in Ni/n-GaN Schottky barrier diode *Appl. Phys. Express* **10** 051002
[12] Nicholls J, Dimitrijev S, Tanner P and Han J 2019 Description and verification of the fundamental current mechanisms in silicon carbide Schottky barrier diodes *Sci. Rep.* **9** 3754
[13] Guo X, Zhong Y, Chen X, Zhou Y, Su S, Yan S, Liu J, Sun X, Sun Q and Yang H 2021 Reverse leakage and breakdown mechanisms of vertical GaN-on-Si Schottky barrier diodes with and without implanted termination *Appl. Phys. Lett.* **118** 243501
[14] Ren B, Liao M, Sumiya M, Wang L, Koide Y and Sang L 2017 Nearly ideal vertical GaN Schottky barrier diodes with ultralow turn-on voltage and on-resistance *Appl. Phys. Express* **10** 051001
[15] Ren J, Yan D, Yang G, Wang F, Xiao S and Gu X 2015 Current transport mechanisms in lattice-matched Pt/Au-InAlN/GaN Schottky diodes *J. Appl. Phys.* **117** 154503
[16] Raja P V, Akhtar J, Rao C V S, Vala S, Abhangi M and Murty N V L N 2017 Spectroscopic performance studies of 4H-SiC detectors for fusion alpha-particle diagnostics *Nucl. Instrum. Methods Phys. Res.* A **869** 118
[17] Ngo T H *et al* 2020 Cathodoluminescence and electrical study of vertical GaN-on-GaN Schottky diodes with dislocation clusters *J. Cryst. Growth* **552** 125911
[18] Tung R T 1992 Electron transport at metal-semiconductor interfaces: general theory *Phys. Rev.* B **45** 13509–23

[19] Lang D V 1979 *Space-charge Spectroscopy in Semiconductors, Thermally Stimulated Relaxation in Solids* (Springer)
[20] Miller G L, Lang D V and Kimerling L C 1977 Capacitance transient spectroscopy *Annu. Rev. Mater. Sci.* **7** 377
[21] Hemmingsson C, Son N T, Kordina O, Bergman J P, Janzén E, Lindström J L, Savage S and Nordell N 1997 Deep level defects in electron-irradiated 4H SiC epitaxial layers *Appl. Phys.* **81** 6155–9
[22] 2017 *Sentaurus TCAD User Guide* Version N-2017.09 (Synopsys Inc.)
[23] Abdelaziz A, Srour H, Hamady S O S, Fressengeas N, Ougazzaden A and Salvestrini J P 2012 Interface state effects in GaN Schottky diodes *Thin Solid Films* **522** 345
[24] Akkal B, Benamara Z, Abid H, Talbi A and Gruzza B 2004 Electrical characterization of Au/n-GaN Schottky diodes *Mater. Chem. Phys.* **85** 27
[25] PhysTech FT-1030 2014 DLTFS manual (PhysTech GmbH)
[26] Raja P V, Bouslama M, Sarkar S, Pandurang K R, Nallatamby J-C, DasGupta N and DasGupta A 2020 Deep-level traps in AlGaN/GaN-and AlInN/GaN-based HEMTs with different buffer doping technologies *IEEE Trans. Electron Devices* **67** 2304
[27] Kamyczek P, Popko E P, Zielony E and Zytkiewicz Z 2013 Deep levels in GaN studied by deep level transient spectroscopy and Laplace transform deep-level spectroscopy *Mater. Sci.* **31** 572
[28] Yamada H, Chonan H, Takahashi T, Yamada T and Shimizu M 2018 Deep-level traps in lightly Si-doped n-GaN on free-standing m-oriented GaN substrates *AIP Adv.* **8** 045311
[29] Chen C-H, Baier S M, Arch D K and Shur M S 1988 A new and simple model for GaAs heterojunction FET gate characteristics *IEEE Trans. Electron Devices* **35** 570
[30] Greco G, Giannazzo F and Roccaforte F 2017 Temperature dependent forward current-voltage characteristics of Ni/Au Schottky contacts on AlGaN/GaN heterostructures described by a two diodes model *J. Appl. Phys.* **121** 045701